Journal of Biomechanics 140 (2022) 111161

Contents lists available at ScienceDirect

Journal of Biomechanics

journal homepage: www.elsevier.com/locate/jbiomech

Distributed lumped parameter modeling of blood flow in compliant vessels

Mehran Mirramezani [*], Shawn C. Shadden

Mechanical Engineering, University of California, Berkeley, CA, 94720, USA

ARTICLE INFO

Keywords:
Reduced order modeling
Deformable blood vessel
Image-based computational fluid dynamics
Wave propagation

ABSTRACT

We extend our previous distributed lumped parameter (DLP) modeling approach to take into account blood vessel wall deformability. This is achieved by adding a compliance term for each vascular segment based on 1D NS equations. The results of the proposed method are compared against 1D Navier–Stokes and 3D fluid–structure interaction (FSI) modeling in idealized and patient-specific models. We show that 1D Navier–Stokes blood flow modeling can be highly inaccurate in predicting flow and pressure dynamics in diseased cases, while in comparison the DLP approach produces consistently accurate flow and pressure waveforms as compared to 3D FSI modeling. The relative accuracy and computational efficiency of the proposed DLP approach offer the possibility to replace or augment 1D or 3D modeling to study hemodynamics in a variety of applications.

1. Introduction

Cardiovascular disease (CVD) is the leading cause of death worldwide. By 2035, it is expected that nearly half of the US population will have some form of CVD, with an associated annual cost of $1.1 trillion (CVD, 2017). Medical imaging is the primary technology for CVD diagnosis and surgical planning. However, imaging on its own provides no predictive capability and limited functional information. Image-based computational fluid dynamics (CFD) (Taylor and Steinman, 2010), the modeling standard to study patient-specific blood flow features in the cardiovascular system, can augment imaging to uncover functional indicators of CVD not revealed through imaging (Taylor et al., 2013; Itu et al., 2013; Arzani and Shadden, 2012; Joly et al., 2018). Moreover, computational modeling provides the ability to virtually test interventions or devices (LaDisa et al., 2003; Sankaran et al., 2012; Bianchi et al., 2018). Despite this upside, patient-specific simulations remain computationally expensive and challenging, and therefore their use in the clinic is limited. These limitations have also been prohibitive in research applications requiring parametric analyses such as uncertainty quantification (Fleeter et al., 2020), data assimilation (Wang et al., 2019), optimization (Marsden, 2014), parameter tuning (Tran et al., 2017), etc. As such, we recently developed a distributed lumped parameter (DLP) framework (Mirramezani and Shadden, 2020), which can compute blood flow and pressure dynamics with substantially reduced computational cost and complexity, but with increased accuracy compared to the existing reduced order models (ROMs) (Toy et al., 1985; Hughes and Lubliner, 1973; Ghigo et al., 2017). This was achieved by proposing a generalized ODE as a "lumped parameter representation" of the governing equation of fluid mechanics in a vessel segment. This ODE can be solved for several elements within each segment of a vascular network to provide a "distributed" understanding of flow and pressure in the network, compared to other lumped parameter (LP) frameworks for which flow and pressure are only computed at vessel junctions and outlets (Chnafa et al., 2017). Another essential aspect of the DLP modeling is that various sources of energy dissipation of blood flow are taken into account to more accurately estimate hydraulic resistance of blood flow by developing analytical expressions based on fundamental fluid flow principles.

DLP modeling provides close predictions for integrated quantities such as pressure drop and flow distribution compared to benchmark CFD simulations at approximately 1/1000 of the computational cost, even in scenarios of complex 3D flow (Mirramezani and Shadden, 2020). However, the DLP framework in Mirramezani and Shadden (2020) does not consider the effects of vessel wall "deformability". Previous studies showed that computed flow and pressure waveforms are discernibly different between rigid and deformable wall assumptions in blood flow modeling (Figueroa et al., 2006). Therefore, phenomenon such as wave propagation, which are known to be important to physiology and diagnostics, are not accessible by such a framework.

Traditionally, the 1D Navier–Stokes (NS) equation (Hughes and Lubliner, 1973) is the conventional reduced order model (ROM) to study hemodynamics, and particularly wave propagation, in compliant vascular networks. However 1D NS models are prone to numerical instability especially for extensive arterial networks (Müller et al., 2016), and are inaccurate for complex flow applications such as vascular stenosis (Mirramezani et al., 2018). Alternatively, detailed analysis

---

[*] Corresponding author.
E-mail address: m.mirramezani@berkeley.edu (M. Mirramezani).

https://doi.org/10.1016/j.jbiomech.2022.111161
Accepted 23 May 2022

of hemodynamics in compliant arteries can be studied by 3D fluid–structure interaction (FSI) simulations (Figueroa et al., 2006; Bazilevs et al., 2009, 2010), but this approach is far more computationally expensive, and this extra cost and complexity is questionable when local intricacies of the flow field do not need to be explicitly known.

Here we develop a computationally efficient method for studying flow and pressure distribution in "deformable" vascular networks by extending the DLP framework presented in Mirramezani and Shadden (2020). In addition to leveraging the modified resistance value in Mirramezani and Shadden (2020), we also propose a compliance term that considers the variation of geometric and material properties of vasculature segments. Specifically this framework is meant to handle complex vascular geometries typical to image-based modeling, where 1D NS models generally provide poor predictions and computationally expensive 3D FSI modeling is therefore typically employed. The results of the proposed method are compared against 1D NS and 3D FSI blood flow modeling for several idealized and image-based vascular models. To the best of our knowledge, this is one of the most comprehensive comparisons of LP and 1D NS modeling to image-based FSI simulations spanning a wide range of healthy, diseased, idealized and patient-specific cardiovascular anatomies with varied geometric and hemodynamic features.

2. Methods

The coupled-momentum method (Figueroa et al., 2006) implemented in SimVascular (Updegrove et al., 2017) was used to model 3D FSI problems. Blood flow was modeled as an incompressible Newtonian fluid with density ρ coupled with the arterial wall that is treated as a thin membrane with linear elastic material properties and density ρ_s. The governing equations for the fluid and solid domains are

$$\begin{aligned} \rho(\mathbf{v}_{,t} + \mathbf{v}\cdot\nabla\mathbf{v}) &= -\nabla p + \nabla\cdot\boldsymbol{\tau}_f \quad \text{in} \quad \Omega^f \\ \nabla\cdot\mathbf{v} &= 0 \quad \text{in} \quad \Omega^f \\ \mathbf{v} &= \mathbf{v}_s \quad \text{on} \quad \Sigma \end{aligned} \tag{1}$$

$$\begin{aligned} \rho_s \mathbf{v}_{s,t} - \nabla\cdot\boldsymbol{\sigma}_s &= 0 \quad \text{in} \quad \Sigma\times h \\ \boldsymbol{\sigma}_s\cdot\mathbf{n}_s &= (-p\mathbf{I} + \boldsymbol{\tau}_f)\cdot\mathbf{n}_s \quad \text{on} \quad \Sigma, \end{aligned} \tag{2}$$

where Ω^f denotes the fluid domain, Σ is the fluid–wall interface, $\mathbf{n}_s$ is the outward normal at Σ, and h is the vessel wall thickness. $\mathbf{v}$ and $\mathbf{v}_s$ are the fluid and solid velocities, respectively, and p is the fluid pressure. $\boldsymbol{\tau}_f$ is the viscous stress tensor of a Newtonian fluid, and $\boldsymbol{\sigma}_s$ is the membrane stress tensor. A stabilized finite element solver with generalized alpha time-stepping scheme in SimVascular was used to solve for blood flow velocity and pressure, and vessel wall deformation.

The "1D" equations representing conservation of mass and balance of momentum for blood flow in a deformable vessel can be expressed as (Sherwin et al., 2003; Milišić and Quarteroni, 2004)

$$\frac{\partial P}{\partial t} + \frac{\partial P}{\partial A}\frac{\partial Q}{\partial x} = 0 \tag{3}$$

$$\frac{\partial Q}{\partial t} + \frac{\partial}{\partial x}\left(\frac{Q^2}{A}\right) + \frac{A}{\rho}\frac{\partial P}{\partial x} + K_r\frac{Q}{A} = 0, \tag{4}$$

where x is the axial coordinate and t is the time. $Q(x,t)$ is the volumetric flow rate, $A(x,t)$ is the cross sectional area of the vessel, $P(x,t)$ is the cross sectionally averaged pressure, and K_r is the viscous friction factor. The following pressure-area relationship was used to complete the system of equations for three unknowns A, Q, and P:

$$P(x,t) = \frac{\beta}{A_d}(\sqrt{A} - \sqrt{A_d}), \qquad \beta = \frac{4}{3}\sqrt{\pi}Eh. \tag{5}$$

E is the vessel wall Young's modulus, and A_d is the diastolic cross sectional area. Using Eq. (5), one has

$$\frac{\partial P}{\partial A} = \frac{\beta}{2A_d\sqrt{A}}. \tag{6}$$

An in-house finite volume solver verified in Mirramezani et al. (2018) was used to solve the above system of equations for the 1D NS equations.

By neglecting the nonlinear convective term in Eq. (4), and then integrating the resulting equations in the x direction we can derive an LP representation of the governing equations for blood flow in a deformable vessel as

$$\left(\int_0^L \frac{2A_d(x)\sqrt{A(x)}}{\beta(x)}dx\right)\frac{d\hat{P}}{dt} + Q_o - Q_i = 0 \tag{7}$$

$$\left(\int_0^L \frac{\rho}{A(x)}dx\right)\frac{d\hat{Q}}{dt} + \mathcal{R}\hat{Q} + P_o - P_i = 0, \tag{8}$$

where Q_o and P_o are flow and pressure at the outlet of each vascular segment while Q_i and P_i are the values at the inlet. $\hat{P} = \frac{1}{L}\int_0^L P(x,t)dx$ and $\hat{Q} = \frac{1}{L}\int_0^L Q(x,t)dx$ are the mean pressure and flow rate in each vascular segment, respectively. Here, in order to close the governing equations we assume $\hat{P} \approx P_i$ and $\hat{Q} \approx Q_o$ (Milišić and Quarteroni, 2004). Eqs. (7) and (8) are analogous to the RLC electrical circuit network, in which

$$C = \int_0^L \frac{2A_d(x)\sqrt{A(x)}}{\beta(x)}dx, \quad L = \int_0^L \frac{\rho}{A(x)}dx, \quad \text{and} \quad R = \mathcal{R}. \tag{9}$$

As vessel stiffness increases, β approaches to a high value and consequently compliance C goes to zero. Taking the rigid wall limit, $\beta \to \infty$, results in equations identical to Eqs. (1) and (2) in Mirramezani and Shadden (2020). As in Mirramezani and Shadden (2020), the generalized resistance $\mathcal{R}$ is obtained by considering various sources of energy dissipation:

$$\begin{aligned} \mathcal{R} = &\underbrace{\frac{8\mu}{\pi}\int_0^L \max\{\gamma,\zeta\}\frac{1}{R^4}dx}_{\text{viscous effect}} + \underbrace{\sum_{i=1}^{n}\frac{\rho K_t}{2A_{0,i}^2}\left(\frac{A_{0,i}}{A_{s,i}} - 1\right)^2|Q|}_{\text{expansions effect}} \\ &+ \underbrace{\frac{1}{2Q}\rho\frac{Q_{dat}^2}{A_{dat}^2}\left(1 + \lambda_j^2\psi_j^2 - 2\lambda_j\psi_j\cos(\phi_j)\right)}_{\text{bifurcation effect}}, \end{aligned} \tag{10}$$

where γ and ζ are curvature and unsteadiness effects, respectively. $K_t = 1.52$ is an empirical correction factor to account for losses at a sudden expansion with minimum A_s and nominal A_0 cross sectional areas. λ_j and ψ_j defines flow and area splits, respectively, and $\phi_j = 3(\pi - \theta_j)/4$ with θ_j is the angle between a datum supplier and a child branch at the bifurcation.

In terms of numerical implementation, we have developed a fully automated framework implemented in Python whose input is a (possibly image-based) vascular network geometry and whose output is a distributed representation of blood flow and pressure computed throughout the geometry. Namely, this framework automatically discretizes each vascular segment to several elements and computes all derived geometric parameters used in the equations above. Eqs. (7) and (8) with appropriate boundary and interface conditions (see Results for examples) are solved in the discretized spatial domain using an implicit Euler time-stepping scheme, which was found to achieve similar accuracy as RK4 with significantly reduced computational cost. The overall DLP modeling workflow is shown in Fig. 1 for an idealized aortic bifurcation model.

3. Results

Here we evaluate the utility of the proposed extended DLP modeling and 1D NS equations against the described (benchmark) 3D FSI modeling in various cardiovascular applications. The same boundary conditions, and mechanical and geometrical properties were used for all three approaches to ensure consistent comparisons. Boundary conditions and material properties for idealized cases are given in Tables 1 and 2. For all image-based models, unknown parameters were

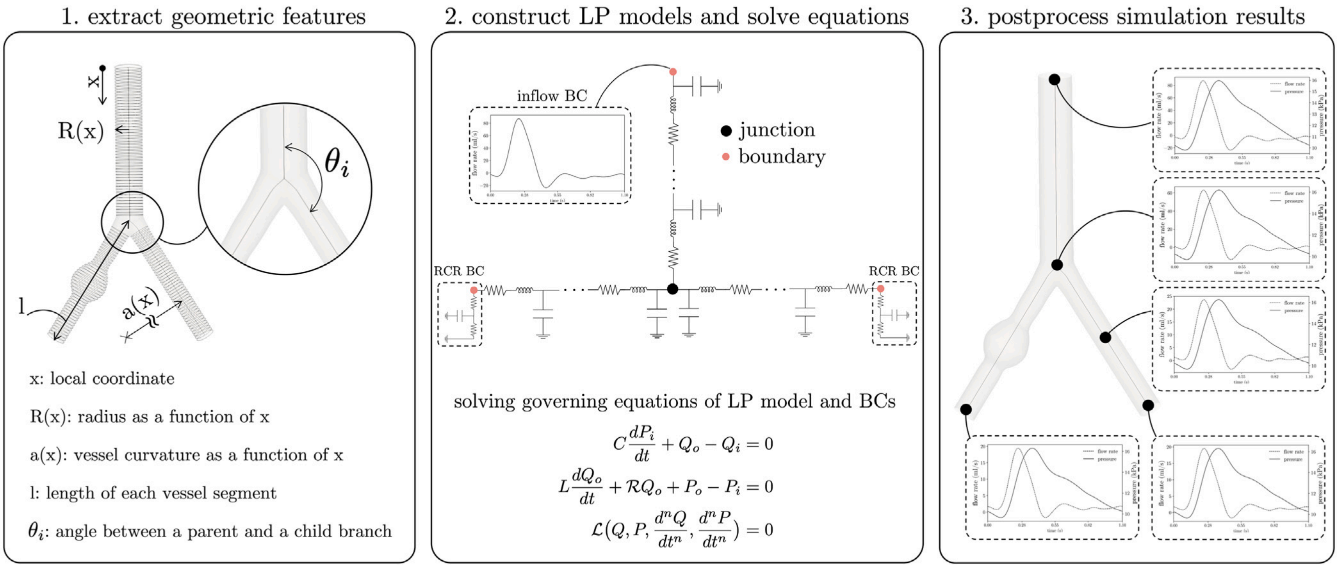

Fig. 1. The modeling steps of the automated DLP framework implemented in Python to compute blood flow and pressure in vasculature networks with deformable vessel walls.

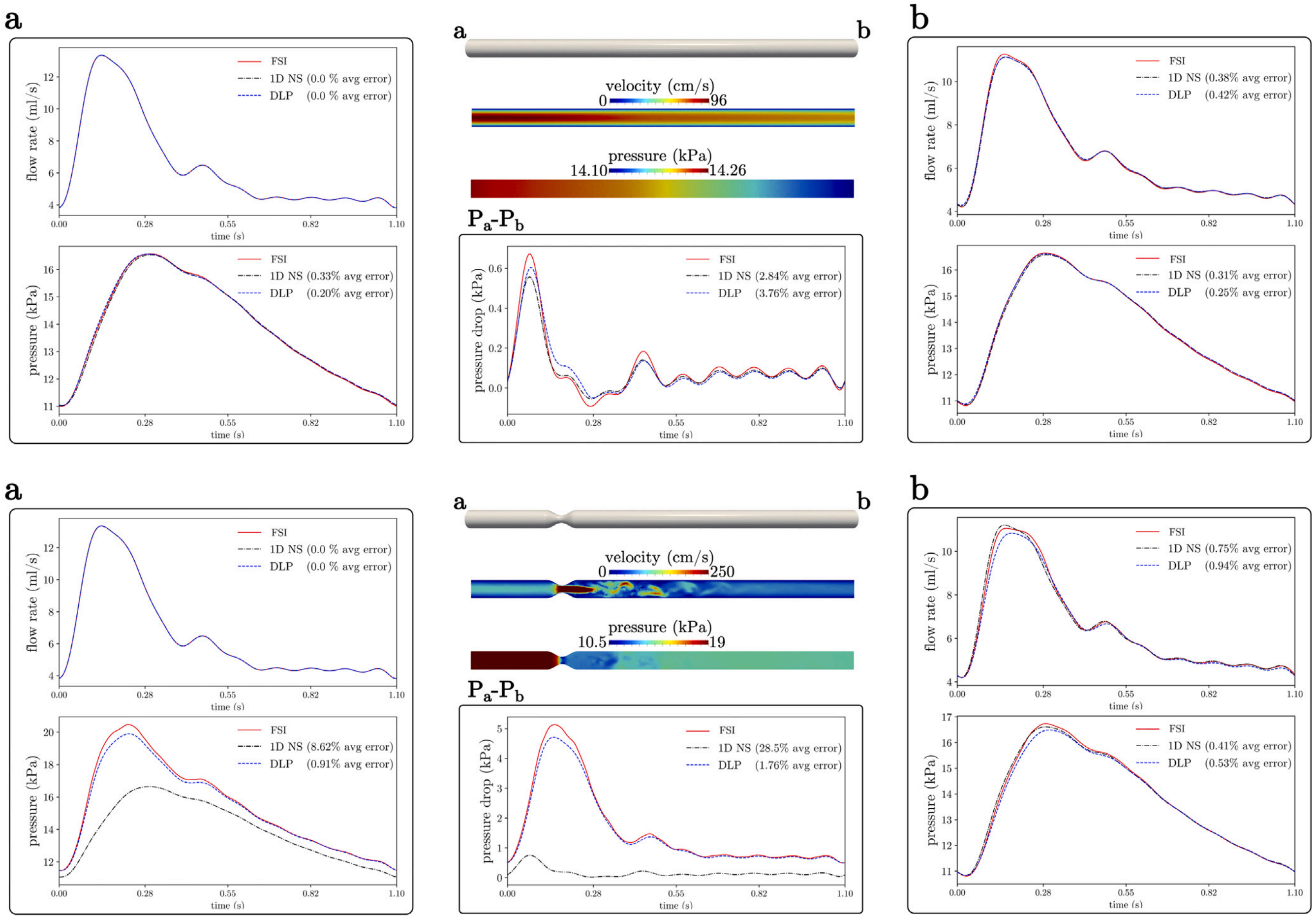

Fig. 2. Pressure and velocity fields in idealized models of a healthy and a stenosed carotid artery during peak systole, and flow rate, pressure, and pressure drop waveforms computed from DLP, 1D NS, and 3D FSI modeling (error values in plot labels).

estimated from known physiological approximations as described next. These parameters should be considered representative for the sake of inter-model comparison, and not patient-specific per se. The pulse wave velocity c was approximated from the empirical relationship $c = 13.3/(2r_d)^{0.3}$ (Milišić and Quarteroni, 2004), where r_d is the diastolic radius. The Young's Modulus for each vascular segment was calculated from Xiao et al. (2014)

$$Eh = \frac{3\rho}{2\sqrt{\pi}} A_d^{\frac{1}{2}} c^2, \tag{11}$$

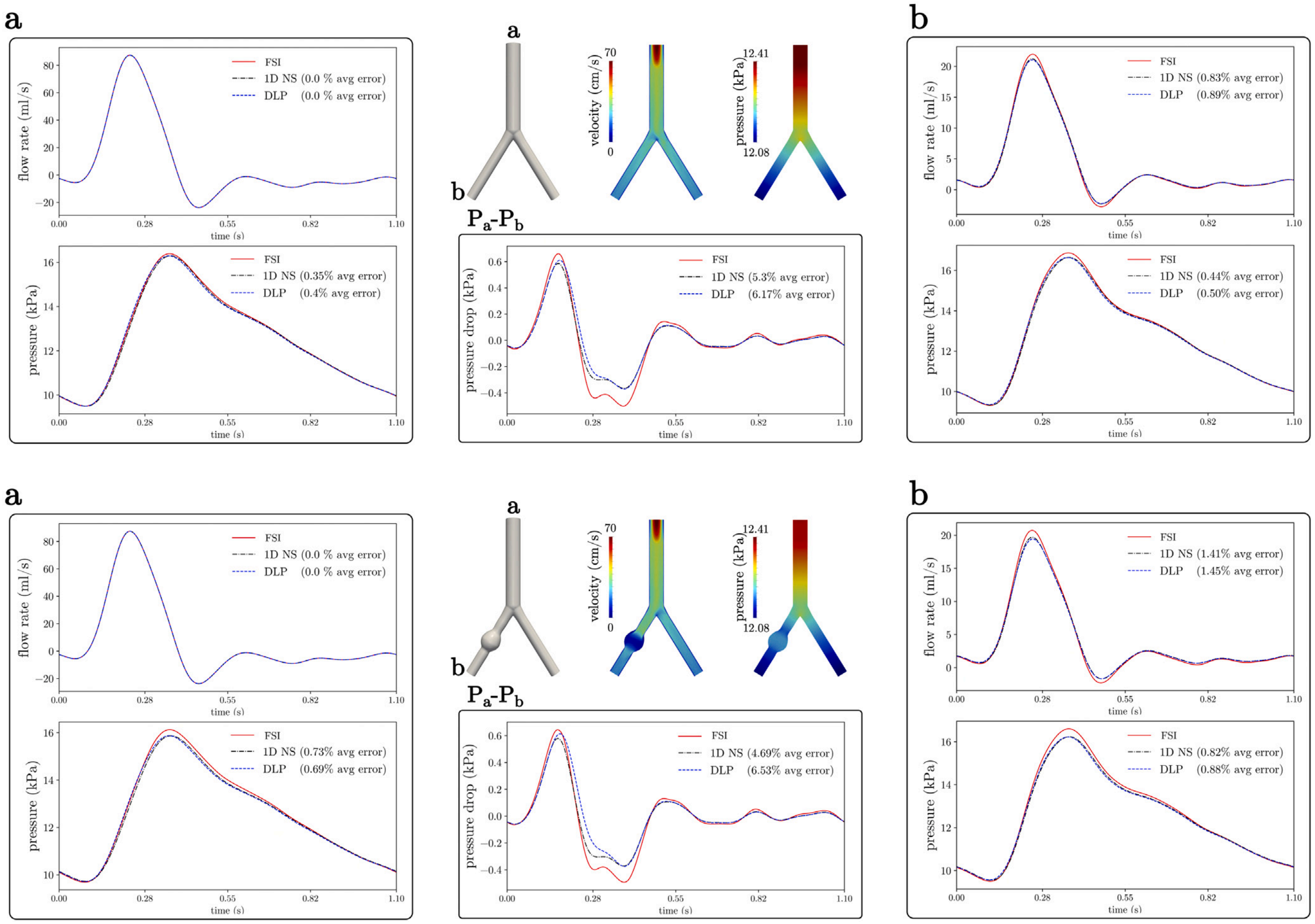

Fig. 3. Pressure and velocity fields in idealized models of a healthy and an aneurysmal aortic bifurcation during peak systole, and flow rate, pressure, and pressure drop waveforms computed from DLP, 1D NS, and 3D FSI modeling (error values in plot labels).

where h is chosen to be 10% of the average r_d in each vascular segment. Parameters of three-element Windkessel outflow boundary conditions were calculated by following the procedure described in Xiao et al. (2014). Namely, a total resistance R_t was obtained from mean blood pressure P_m and total inlet flow rate Q_{in}, i.e., $R_t = P_m/Q_{in}$. The total resistance was distributed between terminal outlets using the principle of flow regulation of vessel size (Kamiya and Togawa, 1980), $R_i = R_t(\sum_{j=1}^{N} A_j/A_i)$ for N outlets. Each individual outlet resistance R_i has a proximal component R_i^p and a distal component R_i^d, where $R_i^p = \rho c_i/(A_d)_i$ to minimize the magnitude of the reflected wave at each outlet. The compliance for each outlet was determined by $C_i = C_p(R_t/R_i^d)$, where C_p is the total arterial peripheral compliance that is calculated from $C_p = C_t - \sum_{j=1}^{M}((A_d)_j l_j)/(\rho c_j^2)$, for M vessels in the network each of which has length l_j. The total compliance was computed as $C_t = \tau/R_t$ with time constant $\tau = 1.79$ s (Simon et al., 1979).

Inlet and outlet pressure and volumetric flow rate data calculated from the extended DLP model and the 1D NS equations were compared with the corresponding data from the 3D FSI simulations using the relative error metrics (Alastruey et al., 2011):

$$e_P = \frac{1}{N_s}\sum_{j=1}^{N_s}\left|\frac{P_j^{ROM} - P_j^{3D}}{P_j^{3D}}\right|, \qquad e_Q = \frac{1}{N_s}\sum_{j=1}^{N_s}\left|\frac{Q_j^{ROM} - Q_j^{3D}}{\max_n(Q_n^{3D})}\right|, \tag{12}$$

where number of time points N_s is chosen to be at least 200 over the last cardiac cycle that all simulations achieved a periodic solution. These error values appear in the graph labels in Figs. 2–7. We note that the flow error is normalized by maximum values from 3D modeling in a cardiac cycle to avoid division by small values close to zero. Mesh independence analysis were performed for all the cases to ensure simulation results from DLP, 1D NS, and 3D FSI modeling were not affected by insufficient mesh resolution. Blood density $\rho = 1060$ kg m^{-3} and viscosity $\mu = 4$ mPa s were assumed common among all models.

3.1. Idealized carotid artery

We considered an idealized vessel with uniform wall properties and geometry representative of a common carotid artery coupled to a three-element Windkessel model with values given in Table 1. A pulsatile flow waveform from Xiao et al. (2014) with a parabolic velocity profile is imposed at the inlet of the model. Fig. 2 (top panel) indicates flow rate, pressure, and pressure drop waveforms predicted from three different modeling approaches. The results from DLP and 1D NS modeling are in strong agreement with 3D FSI simulations where maximum average errors in flow and pressure are less than 0.5%. We alternatively studied the accuracy of these approaches in a diseased carotid artery with ~60% diameter reduction stenosis, which is within the range of a critical stenosis. Fig. 2 (bottom panel) shows that the 1D NS model is significantly inaccurate in predicting pressure waveform at the inlet (with ~9% average error) and pressure drop waveform (with ~30% average error). However, average errors in pressure and pressure drop from DLP modeling are less than 1% and 2%, respectively.

3.2. Idealized aortic bifurcation

An aortic bifurcation model representing the abdominal aorta and iliac arteries is presented here as an idealized model with complex

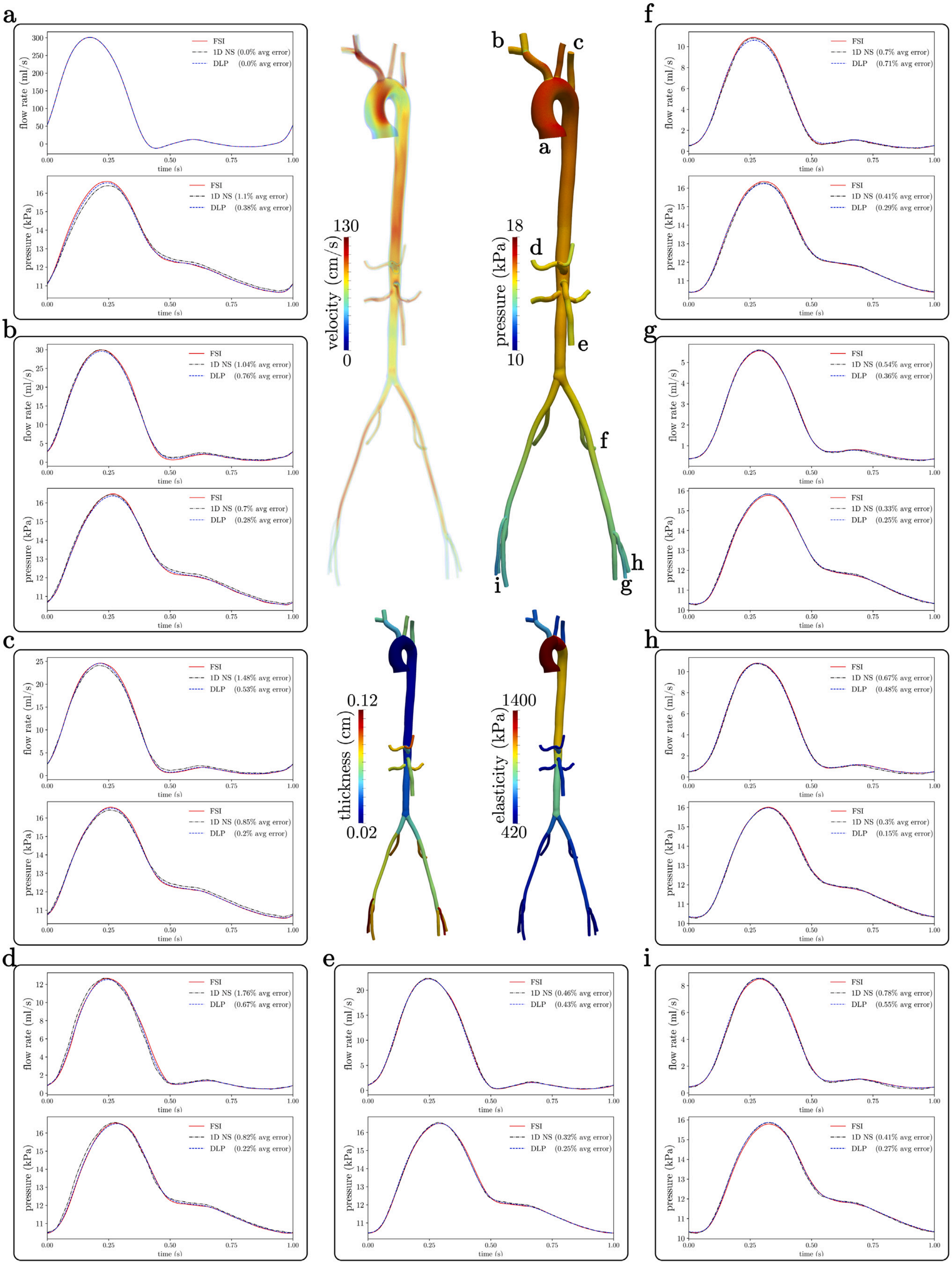

Fig. 4. Pressure and velocity fields of a patient-specific aorta-femoral model, and flow rate and pressure waveforms computed from DLP, 1D NS, and 3D FSI modeling at representative outlets (error values in plot labels).

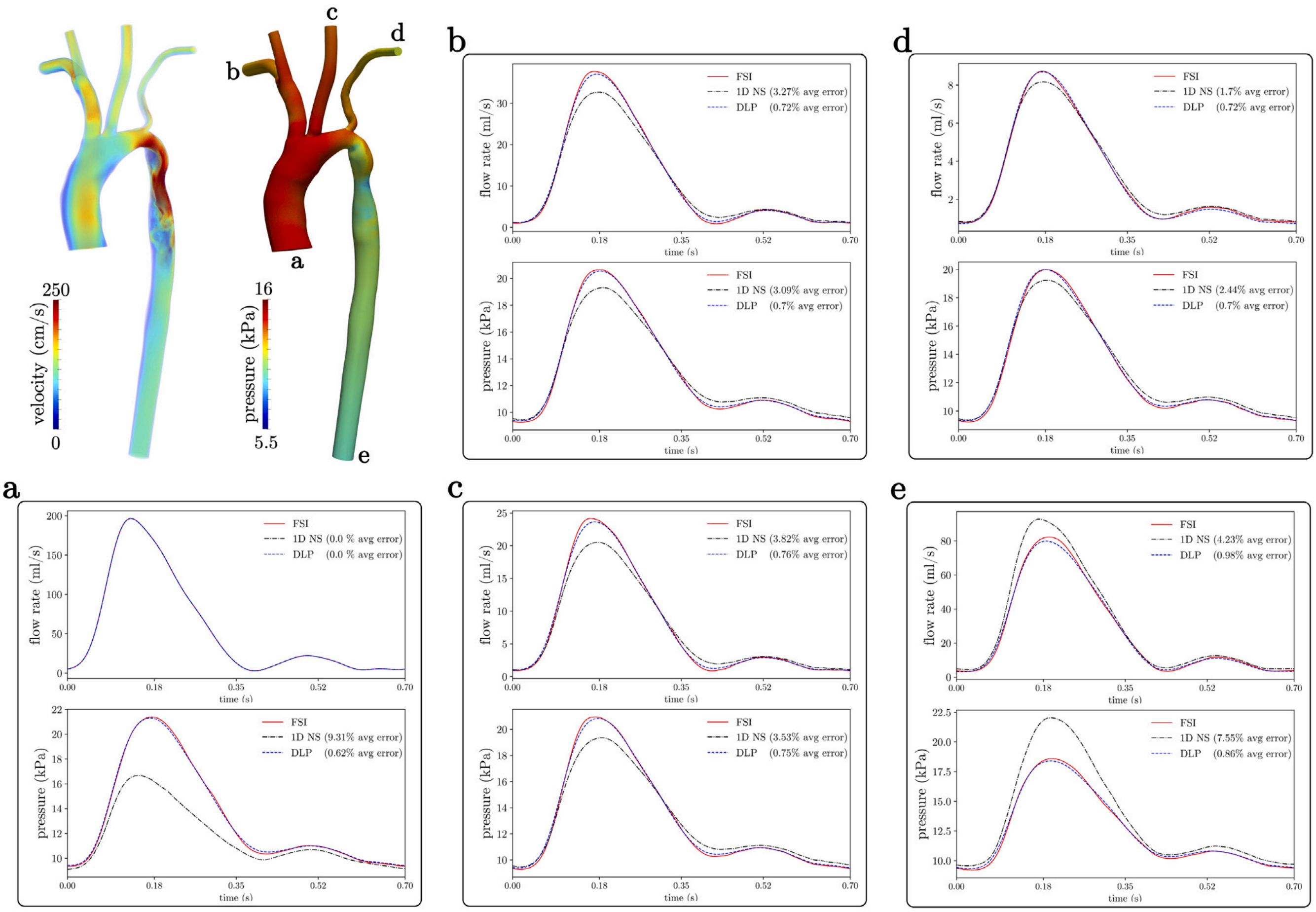

Fig. 5. Pressure and velocity fields of a patient-specific aortic model with mild coarctation, and flow rate and pressure waveforms computed from DLP, 1D NS, and 3D FSI modeling at representative outlets (error values in plot labels).

Table 1
Model parameters of an idealized common carotid artery from Xiao et al. (2014).

Property	Value
Length, L	126 mm
Radius at diastolic pressure, r_d	3 mm
Wall thickness, h	0.3 mm
Young's modulus, E	700 kPa
Diastolic pressure, P_d	10.933 kPa
Windkessel resistance, R_p	2.4875 10^8 Pa s m^{-3}
Windkessel compliance, C	1.7529 10^{-10} m^3 Pa^{-1}
Windkessel resistance, R_d	1.8697 10^9 Pa s m^{-3}

Table 2
Model parameters of an idealized aortic bifurcation from Xiao et al. (2014).

Property	Aorta	Iliac
Length, L	86 mm	85 mm
Radius at diastolic pressure, r_d	8.6 mm	6.0 mm
Wall thickness, h	1.032 mm	0.72 mm
Young's modulus, E	500 kPa	700 kPa
Diastolic pressure, P_d	9.5 kPa	9.5 kPa
Windkessel resistance, R_p	–	6.8123 10^7 Pa s m^{-3}
Windkessel compliance, C	–	3.6664 10^{-10} m^3 Pa^{-1}
Windkessel resistance, R_d	–	3.1013 10^9 Pa s m^{-3}

flow features at a junction. Geometrical and mechanical parameters are listed in Table 2. A similar model with an iliac aneurysm of $\sim$90% dilation in radius was also considered. Fig. 3 (top panel) shows that both DLP and 1D NS modeling are reasonably accurate in computing flow and pressure dynamics for the non-aneurysmal idealized aortic bifurcation model as compared to 3D FSI, where average errors for flow and pressure are less than 1%. Furthermore, and in contrast to the stenotic carotid case presented above, both DLP and 1D NS had almost similar (relatively small, less than 2%) error in computing pressure and flow for the iliac aneurysm case.

3.3. Aortofemoral model

We considered a non-diseased aorta-femoral model with significant spatial extent starting from the ascending aorta to the femoral arteries. A typical aortic flow waveform, adopted to match a mean cardiac output of 4.6 L/min for a female, was imposed at the inlet of the model (Fig. 4(a)). Three-element RCR Windkessel models are coupled at the outlet based on the method described above. The spatially varying wall thickness and elasticity calculated from the procedure described in Section 3 are shown in Fig. 4. The model has complex flow patterns with a wide range of Reynolds number ($\sim 3000 - \sim 700$) and Womersley number ($\sim 13 - \sim 4$). Fig. 4 plots temporal flow rate and pressure waveforms from DLP, 1D NS, and 3D FSI simulations at several locations of the model. The results from ROMs are in strong agreement with FSI modeling. The maximum average error from DLP modeling and 1D NS method are 0.76% and 1.76%, respectively.

3.4. Aortic model

We considered a model of the ascending aorta to the location in the descending aorta just above the diaphragm with a mild coarctation, which is one of the more common congenital cardiovascular defects. An ascending aorta phase-contrast MRI waveform with a period of

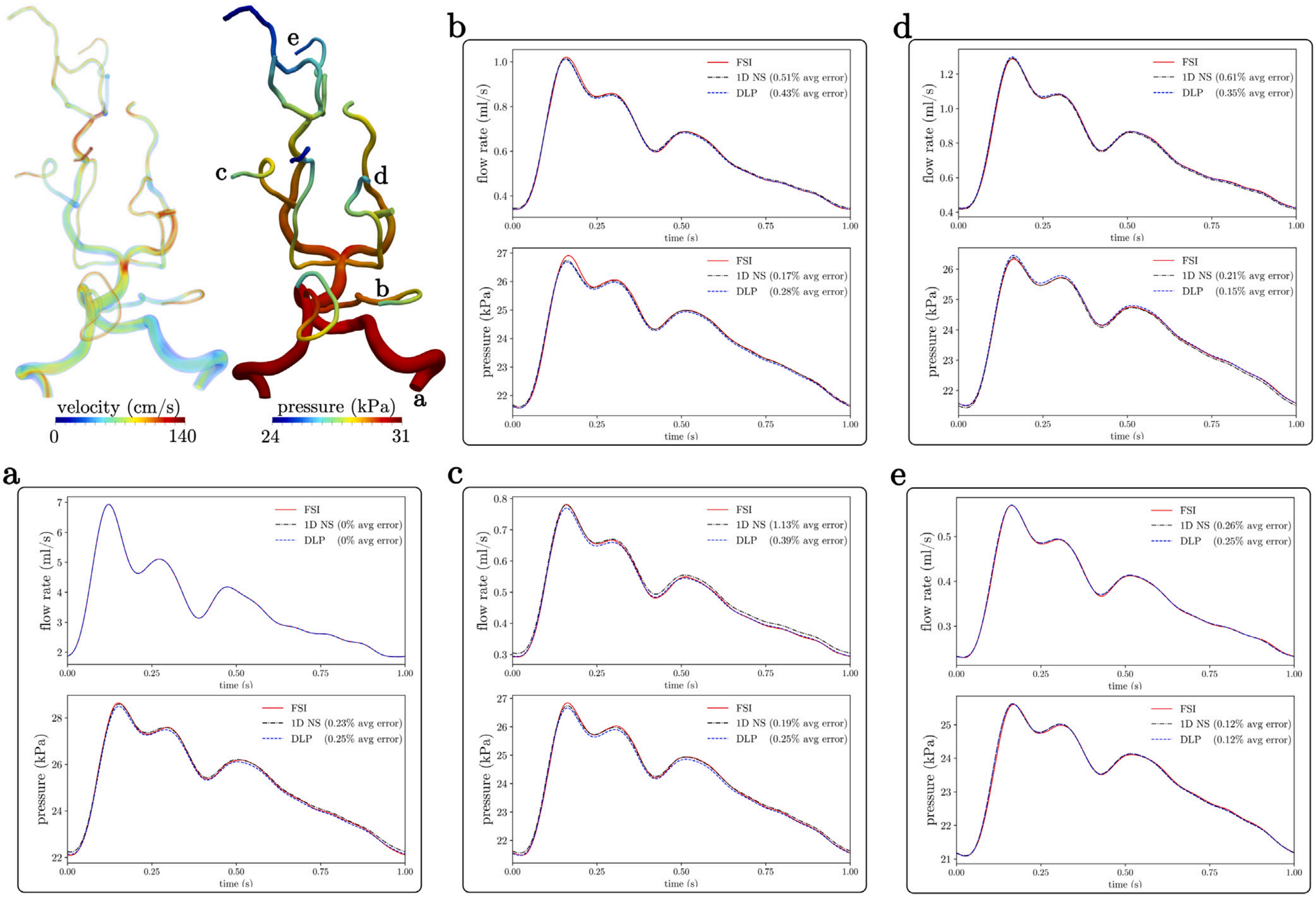

Fig. 6. Pressure and velocity fields of a patient-specific cerebrovascular model, and flow rate and pressure waveforms computed from DLP, 1D NS, and 3D FSI modeling at representative outlets (error values in plot labels).

$T = 0.7$ s was prescribed to the inlet of the computational models, and RCR lumped parameter models were applied at the outlets. Regional mesh refinement was used at the aortic coarctation location in 1D NS and 3D FSI modeling. Fig. 5 illustrates that flow rate and pressure waveforms predicted from 1D NS equations deviate significantly from the 3D FSI results, especially at the inlet and the outlet downstream of the stenotic region with a maximum error of ~10% for inlet pressure. However, the DLP model produces consistently accurate results even in cases of complex flow features, where average error values are less than 1% for computed flow rate and pressure in the model.

3.5. Cerebrovascular model

Here we evaluate the ROM performance for computing hemodynamics in a patient-specific cerebrovascular model with sharp curvature and complex converging and diverging flows at several junctions. A characteristic vertebral flow waveform shown in Fig. 6(a) is employed at the two inlets vertebral arteries. RCR boundary conditions were used at the outlets. The DLP modeling predictions of hemodynamics remain consistent to 3D FSI modeling with a maximum average error less than 0.5% for flow and pressure at representative outlets in Fig. 6. The results of 1D NS modeling are also in good agreement with 3D modeling, with maximum error of 1.13%.

3.6. Coronary model

We considered an image-based model of the aortic root and coronary arteries with a severe stenosis in the first diagonal branch. Coronary blood flow modeling is one of the more complex cardiovascular flow simulations because it is significantly affected by physiology of the heart, which is captured by appropriate boundary conditions. A characteristic aortic flow was prescribed at the root of the aorta and an RCR network was coupled at the aortic outlet. Coronary-specific LP models are coupled at the outlets to consider the influence of intramyocardial pressure on coronary flow (Kim et al., 2010). A detailed description of calculating and tuning of boundary condition parameters is given in Sankaran et al. (2012). Fig. 7 compares flow rate and pressure waveforms computed from ROMs and FSI simulations. The results from DLP method are in strong agreement with FSI modeling even at locations **b** and **c** downstream of the sever stenosis with ~6% and ~4% average error in pressure, respectively. However, the 1D NS modeling cannot accurately capture pressure and flow rate waveforms in locations affected even by a mild stenosis i.e., location **a**. The error values from 1D modeling increases to more than 20% in locations of severe stenosis.

4. Discussion

We extended the application of our previous ROM technique (Mirramezani and Shadden, 2020) to compute integrated hemodynamics quantities in vascular models with compliant walls. Recently Pewowaruk and Roldán-Alzate (Pewowaruk and Roldán-Alzate, 2021) developed a DLP-FSI framework based on Mirramezani and Shadden (2020) to include vessel distensibility in reduced order blood flow modeling. Their framework showed good agreement with analytical solutions of flow, experimental observations, and in vivo measurements. They utilized linear interpolation functions to approximate pressure variation over a vessel based on inlet and outlet pressure values.

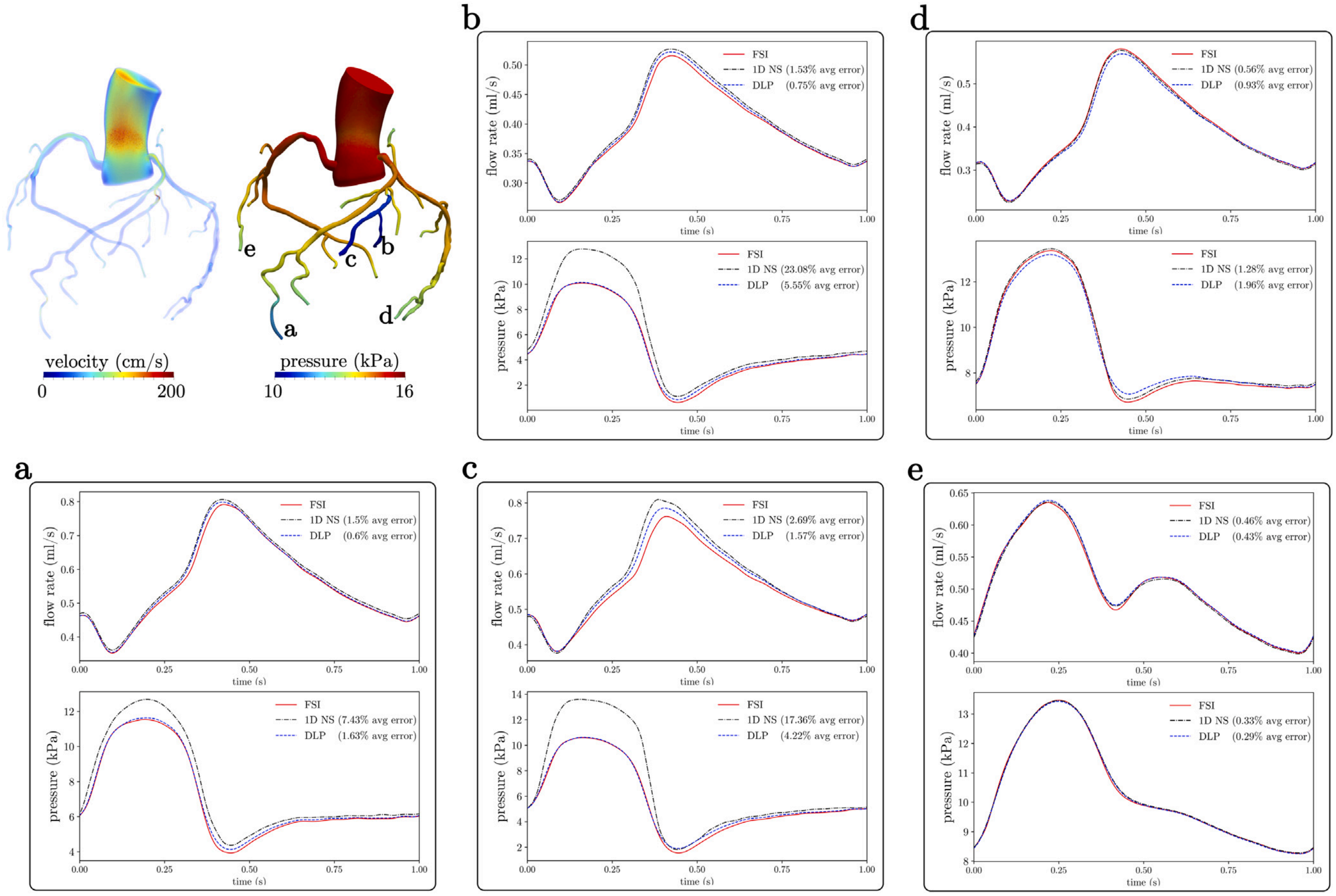

Fig. 7. Pressure and velocity fields of a patient-specific coronary model, and flow rate and pressure waveforms computed from DLP, 1D NS, and 3D FSI modeling at representative outlets (error values in plot labels).

Alternatively, our framework computes inter-vessel pressure values by discretizing each vascular segment to several elements. In addition to this difference among others in methodology, here we focused on comparison of our extended DLP model with other existing numerical solutions of blood flow in vasculature networks with deformable walls. We compared the ability of the proposed DLP model to predict flow rate and pressure waveforms against the long-established 1D NS equations and 3D FSI modeling. Our method provided consistent prediction with 3D time-dependant FSI simulations, and outperformed the 1D NS modeling for several cases with complex flow dynamics such as in stenotic arteries i.e., Section 3.1, Section 3.4, and Section 3.6. This is mainly because energy losses at sudden expansions are not captured in the 1D NS formulation. Our automated framework generally requires 1-order and 3-orders of magnitude less computational cost of 1D NS and 3D FSI simulations, respectively. On a single CPU core, it took 565 ± 22 s to complete 10 cardiac cycles for image-based models, with ~40% of computational cost for solving the governing equations (steps 2 and 3 in Fig. 1) and the rest for extracting geometric features as inputs for the solver (step 1 in Fig. 1).

Given the relative accuracy, numerical stability, computational efficiency, and ease of implementation of the extended DLP approach, it could potentially replace the widely-used 1D NS blood flow modeling in several applications. We showed that the 1D NS equations are significantly unreliable in predicting transstenotic pressure drops stemming from energy losses at sudden expansions (i.e., Section 3.1, Section 3.4, and Section 3.6), which are not captured in the 1D NS formulation. Moreover, in case of stenoses, our in-house 1D solvers experienced stability difficulties that required extremely fine discretization in time and space, which resulted in a remarkable increase of computational effort. We observed this issue in 1D NS modeling using different numerical schemes such as our in-house finite volume solver (Mirramezani et al., 2018) and finite element method (Wan et al., 2002) implemented in https://github.com/SimVascular/svOneDSolver. Previous studies have tried to fix these challenges by coupling the 1D NS equations with LP models to capture pressure losses at sudden expansions (Strocchi et al., 2017). But this approach is problematic for a couple of reasons: First, the coupling procedure is challenging and requires special considerations, making its implementation difficult. Second, the LP model is only used in place of severe stenosis, however, accumulation of pressure drops stemming from mild and moderate stenoses can result in significant changes of flow and pressure distribution in vasculature networks or arteries with diffuse disease.

Previous studies showed accuracy of our prior DLP modeling in several clinical applications such as evaluating the hemodynamic significance of peripheral vascular lesions (Mirramezani et al., 2021), estimating pulmonary artery stenoses pressure drops (Pewowaruk et al., 2021a), predicting outcomes of catheter intervention for branch pulmonary stenoses (Pewowaruk et al., 2021b), and measuring flow distributions in the aorta (Pewowaruk and Roldán-Alzate, 2021). However, there are several other functional indicators of cardiovascular disease that are related to blood vessel wall deformability. For example, changes in blood flow waveform pattern from triphasic to bi/monophasic in peripheral arteries and cerebrovascular arteries indicate the existence of diseases such as stenoses. The proposed extended DLP model can thus be potentially used as a rapid noninvasive tool to study hemodynamic waveforms and their relation to diseases. Moreover, in other applications that require a fully-resolved 3D FSI modeling such as for computing wall shear stress distribution, the extended DLP method can be used for quick initial parameter tuning of 3D simulation to reduce the number of required 3D simulations before achieving the target simulation.

CRediT authorship contribution statement

Mehran Mirramezani: Writing – review & editing, Writing – original draft, Visualization, Methodology, Formal analysis, Conceptualization. **Shawn C. Shadden:** Writing – review & editing, Supervision, Funding acquisition, Formal analysis, Conceptualization.

Declaration of competing interest

The authors declare the following financial interests/personal relationships which may be considered as potential competing interests: Mehran Mirramezani and Shawn C. Shadden have patent applications related to DLP modeling

Acknowledgments

This work was supported in part by the American Heart Association, USA, Award No. 18EIA33900046.

References

2017. Cardiovascular Disease: A Costly Burden for America: Projections Through 2035. Research Triangle Park, NC: Research Triangle Institute.

Alastruey, J., Khir, A.W., Matthys, K.S., Segers, P., Sherwin, S.J., Verdonck, P.R., Parker, K.H., Peiró, J., 2011. Pulse wave propagation in a model human arterial network: Assessment of 1-D visco-elastic simulations against in vitro measurements. J. Biomech. 44 (12), 2250–2258.

Arzani, A., Shadden, S., 2012. Characterization of the transport topology in patient-specific abdominal aortic aneurysm models. Phys. Fluids 24, 081901.

Bazilevs, Y., Hsu, M.C., Benson, D.J., Sankaran, S., Marsden, A.L., 2009. Computational fluid–structure interaction: methods and application to a total cavopulmonary connection. Comput. Mech. 45 (1), 77–89.

Bazilevs, Y., Hsu, M.C., Zhang, Y., Wang, W., Liang, X., Kvamsdal, T., Brekken, R., Isaksen, J.G., 2010. A fully-coupled fluid-structure interaction simulation of cerebral aneurysms. Comput. Mech. 46 (1), 3–16.

Bianchi, M., Marom, G., Ghosh, R., Rotman, O., Parikh, P., Gruberg, L., Bluestein, D., 2018. Patient-specific simulation of transcatheter aortic valve replacement: impact of deployment options on paravalvular leakage. Biomech. Model. Mechanobiol. 18 (2), 435–451.

Chnafa, C., Valen-Sendstad, K., Brina, O., Pereira, V., Steinman, D., 2017. Improved reduced-order modelling of cerebrovascular flow distribution by accounting for arterial bifurcation pressure drops. J. Biomech. 51, 83–88.

Figueroa, C.A., Vignon-Clementel, I.E., Jansen, K.E., Hughes, T.J., Taylor, C.A., 2006. A coupled momentum method for modeling blood flow in three-dimensional deformable arteries. Comput. Methods Appl. Mech. Engrg. 195 (41), 5685–5706, John H. Argyris Memorial Issue. Part II.

Fleeter, C.M., Geraci, G., Schiavazzi, D.E., Kahn, A.M., Marsden, A.L., 2020. Multilevel and multifidelity uncertainty quantification for cardiovascular hemodynamics. Comput. Methods Appl. Mech. Engrg. 365, 113030.

Ghigo, A., Fullana, J., Lagre, P., 2017. A 2D nonlinear multiring model for blood flow in large elastic arteries. J. Comput. Phys. 350, 136–165.

Hughes, T., Lubliner, J., 1973. On the one-dimensional theory of blood flow in the larger vessels. Math. Biosci. 18 (1), 161–170.

Itu, L., Sharma, P., Ralovich, K., Mihalef, V., Ionasec, R., Everett, A., Ringel, R., Kamen, A., Comaniciu, D., 2013. Non-invasive hemodynamic assessment of aortic coarctation: validation with in vivo measurements. Ann. Biomed. Eng. 41 (4), 669–681.

Joly, F., Soulez, G., Garcia, D., Lessard, S., Kauffmann, C., 2018. Flow stagnation volume and abdominal aortic aneurysm growth: Insights from patient-specific computational flow dynamics of Lagrangian-coherent structures. Comput. Biol. Med. 92, 98–109.

Kamiya, A., Togawa, T., 1980. Adaptive regulation of wall shear stress to flow change in the canine carotid artery. Am. J. Physiol.-Heart Circ. Physiol. 239 (1), H14–H21, PMID: 7396013.

Kim, H., Vignon-Clementel, I., Coogan, J., Figueroa, C., Jansen, K., Taylor, C., 2010. Patient-specific modeling of blood flow and pressure in human coronary arteries. Ann. Biomed. Eng. 38 (10), 3195–3209.

LaDisa, J., Guler, I., Olson, L., Hettrick, D., Kersten, J., Warltier, D., Pagel, P., 2003. Three-dimensional computational fluid dynamics modeling of alterations in coronary wall shear stress produced by stent implantation. Ann. Biomed. Eng. 31 (8), 972–980.

Marsden, A., 2014. Optimization in cardiovascular modeling. Annu. Rev. Fluid Mech. 46, 519–546.

Milišić, V., Quarteroni, A., 2004. Analysis of lumped parameter models for blood flow simulations and their relation with 1D models. ESAIM Math. Model. Numer. Anal. 38 (4), 613–632.

Mirramezani, M., Cimadomo, P., Ahsan, E., Shavelle, D., Clavijo, L., Shadden, S.C., 2021. Mathematical modeling of blood flow to evaluate the hemodynamic significance of peripheral vascular lesions. J. Angiol. Vasc. Surg. 6 (76), 16856.

Mirramezani, M., Diamond, S., Litt, H., Shadden, S., 2018. Reduced order models for transstenotic pressure drop in the coronary arteries. J. Biomech. Eng. 141 (3), 031005.

Mirramezani, M., Shadden, S.C., 2020. A distributed lumped parameter model of blood flow. Ann. Biomed. Eng. 48 (12), 2870–2886.

Müller, L.O., Blanco, P.J., Watanabe, S.M., Feijóo, R.A., 2016. A high-order local time stepping finite volume solver for one-dimensional blood flow simulations: application to the ADAN model. Int. J. Numer. Methods Biomed. Eng. 32 (10), e02761, e02761 cnm.2761.

Pewowaruk, R., Lamers, L., Roldán-Alzate, A., 2021a. Accelerated estimation of pulmonary artery stenosis pressure gradients with distributed lumped parameter modeling vs. 3D CFD with instantaneous adaptive mesh refinement: Experimental validation in swine. Ann. Biomed. Eng..

Pewowaruk, R., Ralphe, J., Lamers, L., Roldán-Alzate, A., 2021b. Non-invasive MRI derived hemodynamic simulation to predict successful vs. unsuccessful catheter interventions for branch pulmonary artery stenosis: Proof-of-concept and experimental validation in swine. Cardiovasc. Eng. Technol..

Pewowaruk, R., Roldán-Alzate, A., 2021. A distributed lumped parameter model of blood flow with fluid-structure interaction. Biomech. Model. Mechanobiol..

Sankaran, S., Moghadam, M., Kahn, A., Tseng, E., Guccione, J., Marsden, A., 2012. Patient-specific multiscale modeling of blood flow for coronary artery bypass graft surgery. Ann. Biomed. Eng. 40 (10), 2228–2242.

Sherwin, S., Franke, V., Peiro, J., Parker, K., 2003. One-dimensional modelling of a vascular network in space-time variables. J. Eng. Math. 47 (3), 217–250.

Simon, A.C., Safar, M.E., Levenson, J.A., London, G.M., Levy, B.I., Chau, N.P., 1979. An evaluation of large arteries compliance in man. Am. J. Physiol.-Heart Circ. Physiol. 237 (5), H550–H554, PMID: 495760.

Strocchi, M., Contarino, C., Zhang, Q., Bonmassari, R., Toro, E., 2017. A global mathematical model for the simulation of stenoses and bypass placement in the human arterial system. Appl. Math. Comput. 300, 21–39.

Taylor, C., Fonte, T., Min, J., 2013. Computational fluid dynamics applied to cardiac computed tomography for noninvasive quantification of fractional flow reserve: scientific basis. J. Am. Coll. Cardiol. 66 (22), 2233–2241.

Taylor, C., Steinman, D., 2010. Image-based modeling of blood flow and vessel wall dynamics: Applications, methods and future directions. Ann. Biomed. Eng. 38, 1188–1203.

Toy, S., Melbin, J., Noordergraaf, A., 1985. Reduced models of arterial systems. IEEE Trans. Biomed. Eng. 32, 174–176.

Tran, J., Schiavazzi, D., Ramachandra, A., Kahn, A., Marsden, A., 2017. Automated tuning for parameter identification and uncertainty quantification in multi-scale coronary simulations. Comput. Fluids 142, 128–138.

Updegrove, A., Wilson, N., Merkow, J., Lan, H., Marsden, A., Shadden, S., 2017. Simvascular: An open source pipeline for cardiovascular simulation. Ann. Biomed. Eng. 45 (3), 525–541.

Wan, J., Steele, B., Spicer, S.A., Strohband, S., Feijoo, G.R., Hughes, T.J., Taylor, C.A., 2002. A one-dimensional finite element method for simulation-based medical planning for cardiovascular disease. Comput. Methods Biomech. Biomed. Eng. 5 (3), 195–206, PMID: 12186712.

Wang, J.-X., Hu, X., Shadden, S.C., 2019. Data-augmented modeling of intracranial pressure. Ann. Biomed. Eng. 47 (3), 714–730.

Xiao, N., Alastruey, J., Alberto Figueroa, C., 2014. A systematic comparison between 1-D and 3-D hemodynamics in compliant arterial models. Int. J. Numer. Methods Biomed. Eng. 30 (2), 204–231.